Available online at www.sciencedirect.com
ScienceDirect
International Journal of Heat and Fluid Flow 28 (2007) 145–160
International Journal of HEAT AND FLUID FLOW
www.elsevier.com/locate/ijhff

Experiments on the turbulent wake of a flat plate in a strong adverse pressure gradient

M.J. Tummers [a,*], D.M. Passchier [b], P.G. Bakker [b]

[a] Delft University of Technology, Faculty of Applied Sciences, P.O. Box 5046, 2600 GA Delft, The Netherlands
[b] Delft University of Technology, Faculty of Aerospace Engineering, P.O. Box 5058, 2600 GB Delft, The Netherlands

Received 1 February 2005; received in revised form 13 February 2006; accepted 22 February 2006
Available online 2 May 2006

Abstract

The wake of a flat plate was subjected to an adverse pressure gradient of sufficient strength to cause local mean-flow reversal. The mean-flow and turbulence statistics were determined with a three-component laser Doppler anemometer. The experimental data were used to determine balances of the momentum equation and the turbulence kinetic-energy equation. The latter showed that the production of turbulence kinetic energy remained at a constant high level whereas the dissipation decreased when moving past the trailing edge into the wake. As a consequence, the turbulence kinetic energy becomes very high in the wake. Spectral density functions measured at various locations in the wake indicate that turbulence kinetic energy accumulates in the very low-frequency range. It is suggested that this is due to the formation of unsteady roll cells in the trailing-edge region.

Keywords: High-lift aerodynamics; Turbulent wake; Adverse pressure gradient

1. Introduction

This investigation of an adverse pressure-gradient wake is related to one particular feature of high-lift aerodynamics, i.e. the development of the wake of the main element in the pressure field that is induced by the flap. An accurate numerical prediction of the near wake of the main element is highly desirable because it has a significant effect on the lift, especially at high incidence. However, as was shown by Adair and Horne (1989) and Nakayama et al. (1990), this wake is extremely complex owing to the combined effects of curvature, asymmetry, streamwise pressure gradients and the interaction between the wake and the boundary layer on the flap. In a most interesting series of wind-tunnel tests on a multi-element airfoil, Petrov (1980) showed that the wake of the main element can exhibit a region with mean-flow reversal that is detached from the surfaces of the various elements (see Fig. 1). Petrov called this phenomenon "detached separation," because the backflow region is separated from the surfaces of the elements by a relatively thin zone that consists of an attached boundary layer and a region of potential flow. Perhaps "free separation" or "off-body separation" is a better label, because "detachment" usually refers to the location in a separating turbulent boundary layer where the wall-shear stress vanishes (Simpson et al., 1981).

The free-separation phenomenon is interesting since it does not occur in flows about single-element airfoils where separation takes place on the surface of the airfoil. The stall of a multi-element airfoil is not always caused by boundary-layer separation on the flap or the aft portion of the main element. The stall can also occur when a zone of reversed flow in the wake of the main airfoil rapidly widens and propagates upstream. In fact, due to the thickening of this main-airfoil wake, the boundary-layer separation on the flap, which occurred at moderate angles of attack in Petrov's experiment, disappeared with increasing incidence.

* Corresponding author. Tel.: +31 152 782477; fax: +31 152 781204.
E-mail address: mark@ws.tn.tudelft.nl (M.J. Tummers).

0142-727X/$ - see front matter © 2006 Elsevier Inc. All rights reserved.
doi:10.1016/j.ijheatfluidflow.2006.02.028

Nomenclature

a_{sp}	structural parameter ($= \overline{u'v'_s}/k$)
C_f	skin-friction coefficient ($= 2\tau_w/(\rho U_e^2)$)
C_p	static-pressure coefficient
H	shape factor ($= \delta^*/\theta$)
k	turbulence kinetic energy
n	coordinate normal to plate surface
P_k	production of turbulence kinetic energy
$\overline{p}_m$	measured static pressure
R_θ	Reynolds number based on momentum thickness
r	radius of curvature
s	coordinate along surface of flat plate
U_e	velocity at edge of shear layer
U_{ref}	free stream velocity
$\overline{u'v'}$	Reynolds shear stress
$\overline{u'v'_s}$	Reynolds shear stress in streamline coordinates
$\overline{u'^2}$	Reynolds normal stress for x-direction
$\overline{v'^2}$	Reynolds normal stress for y-direction
x	coordinate along wind-tunnel axis
y	lateral coordinate
δ^*	displacement thickness
ϵ	dissipation rate
θ	momentum thickness
κ	Von Karman constant
ν	kinematic viscosity
τ_w	wall-shear stress
ω	radial frequency

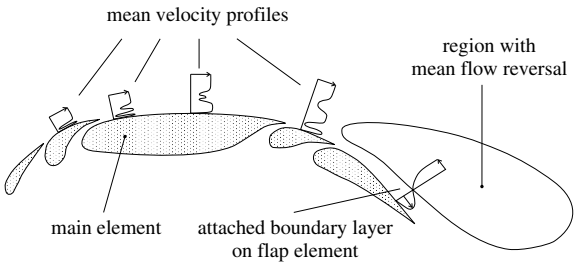

Fig. 1. Illustration of free-separation in the flow around a multi-element airfoil as observed by Petrov (1980).

Consequently, the flow on the flap and on the main element remained fully attached during the stall. This was also reported by, for example, Johnston and Horton (1986).

There are only a few investigations of the free-separation phenomenon, despite its practical significance in high-lift aerodynamics or other technical applications in which free shear layers are subjected to severe streamwise pressure gradients. Over the past decade the phenomenon has attracted some attention as evidenced by the work of Liu et al. (2002), Driver and Mateer (2002), Hoffenberg and Sullivan (1998) and Tummers et al. (1997). An interesting early contribution is the experiment performed by Hill et al. (1963), who investigated the effects of streamwise pressure gradients on the decay of wakes. They subjected the wake of a thick plate with a streamlined nose to adverse pressure gradients of various strengths by means of a diffusing wind-tunnel section with variable side walls. The experiments of Hill et al. (1963) showed that the maximum velocity defect in an adverse pressure-gradient wake decreases at a slower rate than in the constant-pressure wake of the same body. For a sufficiently strong pressure gradient, the maximum velocity defect increased rather than decreased, so that a zone of reversed mean flow developed in the central portion of the wake. This backflow region is not attached to the surface of the wake generating body.

The present investigation can be considered as a follow-up of the study carried out by Hill et al. (1963). It focuses on the development of the near wake of an "airfoil-like" flat plate that is subjected to a strong adverse pressure gradient. The pressure distribution was tuned such that the boundary layer at the trailing edge of the plate was close to separation. This simulates the trailing-edge flow on the suction side of an airfoil near maximum lift. A zone with mean-flow reversal occurred some distance downstream of the trailing edge of the plate. As in the experiment of Hill et al. (1963), the recirculation zone was not attached to the surface of the plate, so that it can be considered a simulation of free separation in the flow about a multi-element airfoil. An important objective of this work is to provide understanding of the free separation in the wake by a thorough analysis of experimental results. The experimental data presented here go beyond the mean velocity and Reynolds stress data, and include several terms in the turbulent kinetic energy equation and spectral density functions.

2. Experimental investigation

2.1. Wind-tunnel and model geometry

The experimental facility used is an open-circuit wind tunnel at the Low-Speed Aerodynamics Laboratory of Delft University of Technology. A centrifugal fan accelerates the air which passes through a diffusing section, the settling chamber and the contraction (1:8) before it reaches the test section with dimensions $400 \times 400\ mm^2$. The test section is followed by a plane diffuser that is made from perspex to allow optical access. The diffuser has a length of 920 mm and the side walls include a 15° angle. To prevent boundary-layer separation along the diffuser walls, a screen was placed at the outlet of the channel and the diffuser walls were equipped with regularly spaced slots. A straight duct with a length of 1000 mm was placed between the diffuser and the screen. The screen induces an

over-pressure inside the channel which causes the boundary layers that develop on the diffuser walls to be blown out through the slots. The absence of flow separation at the diffuser walls was confirmed with tufts and by a flow visualisation using a laser light sheet and oil smoke.

An airfoil-like flat plate with a 600 mm chord and a thickness of 18 mm served as a wake generator. The plate has an elliptic nose and the last 116 mm were tapered to form a sharp trailing edge with a thickness of approximately 0.2 mm. The change in the surface contour from the constant-thickness region of the plate to the tapered region was rounded to avoid flow separation. The model was placed at zero incidence in the test section of the wind tunnel, and the aft portion of the plate (50% chord) was located in the diffuser as shown in Fig. 2. The boundary layers on both sides of the plate were tripped with wires to ensure uniform laminar-to-turbulent transition across the span. The wires had a diameter of 1 mm and were positioned at 6% chord from the leading edge. The divergence of the diffuser and the width of the slots in the diffuser walls were tuned such that the turbulent boundary layers at the trailing edge of the plate were nearly separated (the shape factor $H \equiv \delta^*/\theta = 2.91$).

Throughout this work an orthogonal coordinate system (x, y, z) will be used with its origin at the trailing edge of the plate at mid span (see Fig. 3). The x-coordinate is measured along the wind-tunnel axis and taken positive in the streamwise direction. The z-coordinate is measured in the spanwise direction and taken positive in the upward direction. A second orthogonal system (s, n, z) is used for measurements in the boundary layer on the tapered region of the plate. The z-coordinate is identical to the one mentioned above. The n-coordinate is measured normal to the plate surface.

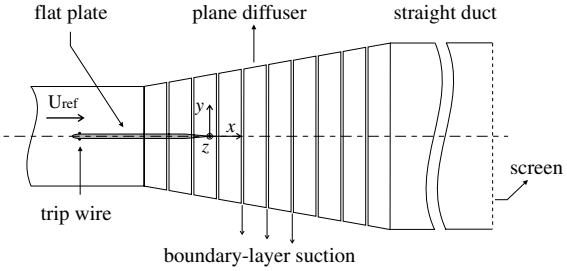

Fig. 2. Top view of the test configuration for the investigation of the wake in adverse pressure gradient.

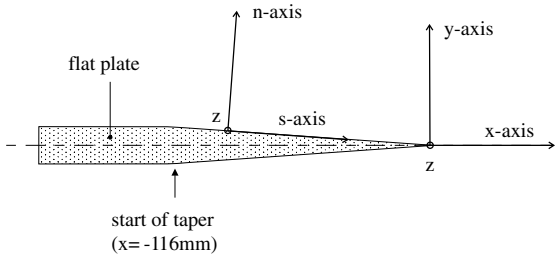

Fig. 3. Definition of the two coordinate systems in the trailing-edge region of the plate.

2.2. Optical arrangements and instrumentation

The single-point statistics were measured with an orthogonal, three-component LDA system. The complete LDA was mounted on a rigid frame that spans the wind tunnel (see Fig. 4). A traversing mechanism enabled displacements of the frame in steps of 5 μm. The green (514.5 nm), blue (488.0 nm) and violet (476.5 nm) colours of a 5 W argon-ion laser were used to measure the three components of the velocity simultaneously. A modular-optics TSI system employed the blue and green colours to measure two velocity components in the x, y-plane. One beam of each colour was frequency shifted over 40 MHz by Bragg cells to enable detection of instantaneous flow reversals. A fibre-optic Dantec LDA used the violet colour to measure the velocity component in the z-direction, i.e. the spanwise velocity component. This LDA channel also included a Bragg cell to introduce an optical shift of 40 MHz.

The three fringe patterns have a nominally orthogonal orientation. The fringe spacings and the precise orientation of the fringe patterns in the x, y, z-coordinate system were determined with a theodolite using procedures similar to those described by Absil (1995). The receiving optics were placed in a plane perpendicular to the optical axes of the transmitting optics, i.e. a side-scatter configuration was used for each channel. This was done to collect scattered light from the overlap region of the three measuring volumes only.

The collected light was separated using a dichroic mirror before it was focused on separate photomultipliers. Each photomultiplier was equipped with a small pinhole which resulted in a reduction of the effective length of the measuring volumes to 0.2 mm. The receiving optics for the violet channel included a 110 mm aperture lens and a small pinhole was placed in front of the photomultiplier to reduce

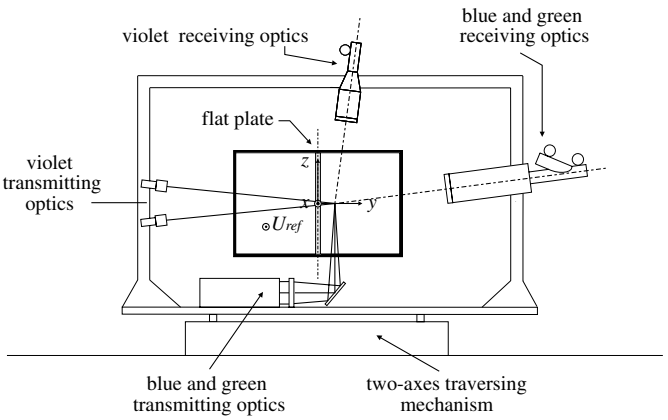

Fig. 4. Experimental set-up for 3-D single-point statistics.

the effective length of the violet measuring volume to about 0.2 mm. Cross talk between the blue, green and violet channels was eliminated by narrow-band optical filters placed in front of each photomultiplier. Note that the small pinholes in conjunction with the side-scatter configuration act as spatial filters that limit the probe size of the 3-D LDA to $0.2 \times 0.2 \times 0.2$ mm^3.

The photomultiplier output signals were electronically down-mixed to an effective frequency pre-shift of 5 MHz and then fed to one Dantec BSA model 57N10 (clock master) and two BSAs model 57N35 (clock slaves). These processors were operated in the "hardware coincident mode", which means that the Doppler signals were processed only when signals were detected on all three channels simultaneously. This mode of operation is needed to ensure that each BSA analyses Doppler bursts that originate from the same particle. Some of the Doppler bursts that pass this hardware-coincidence test are rejected by the internal validation procedures performed by each processor. Since the processors apply the internal validation test independently of each other, it is possible that from triplets of hardware coincident Doppler bursts only one or two bursts are validated. Therefore, a conventional (software) time-coincidence window has to be applied during the later data reduction on a computer.

An air-blast atomizer was used to seed the flow with small oil droplets (Rizella oil). The size distribution of the droplets was measured (Plomp, 1986), and found to have an average value of 0.98 μm, while 95% of the particles were smaller than 2.0 μm. The droplets were injected into the flow upstream of the centrifugal fan to ensure a homogeneous distribution in space.

The test section speed U_{ref} is used to make all measured data dimensionless. The experiments were performed at a constant chord-based Reynolds number of 4×10^5, corresponding to a test-section speed of about 10.2 m/s. When atmospheric conditions changed, small adjustments of the test-section speed were made in between measurement runs (but not during the runs) to maintain the constant Reynolds number.

2.3. Measuring programme and data reduction

Single-point statistics were measured in the wake of the plate on a grid consisting of a centreline traverse and six lateral traverses located between $x = 17$ mm and $x = 175$ mm. In addition, the boundary layer in the trailing-edge region was surveyed with five traverses located between $x = -137$ mm and the trailing edge ($x = 0$ mm). Each wake traverse consisted of approximately 60 measurement stations, whereas the number of stations per boundary layer traverse was slightly less, about 50. At each measurement location at least 2×10^4 velocity samples were acquired with the 3-D LDA. During these measurements the mean data rate varied between 200 Hz in the outer regions of the shear layer and 25 Hz near the centreline or close to the walls. The velocity samples were used to calculate the mean-velocity components ($\overline{u}$, $\overline{v}$ and $\overline{w}$), the Reynolds stresses ($\overline{u'^2}$, $\overline{v'^2}$, $\overline{w'^2}$ and $\overline{u'v'}$), and the triple-velocity correlations ($\overline{u'^3}$, $\overline{u'v'^2}$, $\overline{u'w'^2}$, $\overline{v'u'^2}$, $\overline{v'^3}$ and $\overline{v'w'^2}$).

All single-point statistics were calculated using the 3D inverse-velocity weighting to compensate for the effects of the velocity bias. In other words: $\omega_i = (u_i^2 + v_i^2 + w_i^2)^{-1/2}$ was used as a weighting factor because the three velocity components were measured simultaneously in an approximately spherical measuring volume.

The overall uncertainty in the measured statistical quantities is as follows (see Absil (1995) for a detailed analysis of the various error sources). The mean-velocity components are accurate up to $\pm 1\%$ of U_{ref}. The Reynolds normal stresses and the Reynolds shear stress are accurate up to $\pm 5\%$ and $\pm 8\%$ of their local maximum values, respectively. The uncertainty in the triple-velocity correlations is about $\pm 20\%$ of the local maximum value.

3. Results and discussion

3.1. Pressure distribution

Pressure measurements were performed in the undisturbed flow outside the wake using a standard static-pressure probe. Static pressures were not measured in the wake itself, because of the high local turbulence intensities. The measurements were taken along a line given by $y = 130.0 + 0.14x$, where x and y were measured in mm. This is approximately a streamline well outside the wake. The static pressures were also measured along a number of lines $x =$ constant to determine the lateral pressure gradient. The measurements allowed an accurate interpolation of the static-pressure distribution along the edge of the computational domain at $y = 200$ mm.

The distribution of the static-pressure coefficient, $C_p \equiv 2(\bar{p} - \bar{p}_{\text{ref}})/(\rho U_{\text{ref}}^2)$, along the line $y = 200$ mm is shown in Fig. 5. It is seen that the adverse pressure gradient gradually decreases in the downstream direction. For larger trailing-edge distances ($x > 400$ mm) the pressure gradient

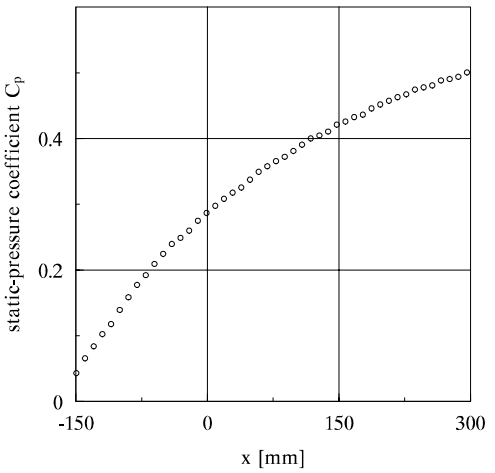

Fig. 5. Static-pressure distribution at $y = 200$ mm.

becomes effectively zero. The pressure distribution was tuned such that a region with mean-flow reversal forms some distance downstream of the trailing edge. Due to the relaxation of the pressure gradient further downstream, the mean flow accelerates again thus forming a 'separation bubble'. There is no mean-flow reversal in the straight channel following the diffusing section.

3.2. Mean-flow characteristics

3.2.1. Mean-velocity components and integral parameters

Fig. 6 shows the three components of the mean velocity measured at station $x = 53$ mm. The centreline velocity is small, but there is not yet mean-flow reversal at this station. Outside the wake, the transverse component shows an increase in the positive y-direction. This is a consequence of the flow developing in a diffusing tunnel section, because according to the continuity equation a decrease of $\bar{u}$ in the x-direction causes an increase of $\bar{v}$ in the y-direction. The continuity equation together with the measured static-pressure distribution were used to compute the value of $\partial\bar{v}/\partial y$ at location $x = 53$ mm, $y = 100$ mm. The solid line in Fig. 6 shows the inferred distribution of $\bar{v}$ (matched at $y = 100$ mm) outside the wake, i.e.,

$$\bar{v} = \bar{v}_m + \frac{\partial \bar{v}}{\partial y} y = \bar{v}_m - \frac{y}{\rho \bar{u}_m} \frac{\partial \bar{p}}{\partial x}, \quad (1)$$

where the subscript m denotes a measured value at location $x = 53$ mm, $y = 100$ mm. The good agreement between the measured and the inferred $\bar{v}$-distribution indicates two-dimensional mean flow. The spanwise velocity, $\overline{w}$, is smaller than 1.6% of the edge velocity at all locations. This is another indication for two-dimensional mean flow. Furthermore, it is seen that the mean flow is reasonably symmetric.

The streamwise development of the x-component of the mean velocity is shown in Fig. 7. The five stations in the upper half of the graph were measured in the boundary layer of the plate. The boundary layer at the station furthest upstream ($x = -137$ mm) has a displacement thickness $\delta^* = 3.7$ mm and a shape factor $H = 1.62$. The thickness of the boundary layer rapidly increases owing to the large pressure rise, and near the trailing edge the velocity profiles develop an inflexion point. The boundary layer is still attached at the trailing edge. There, the characteristics of the mean-velocity profile are $H = 2.91$ and $\delta^* = 18.9$ mm.

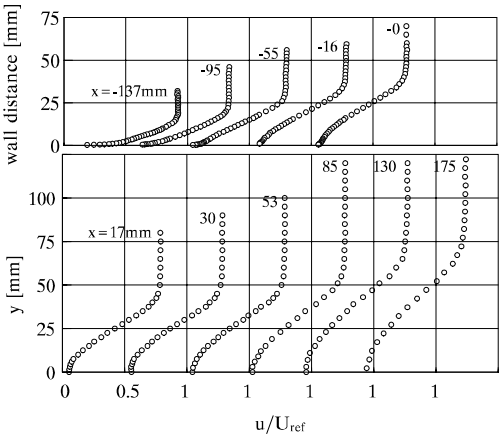

Fig. 7. Streamwise development of the x-component of the mean velocity. Top: boundary layer, bottom: wake.

A more detailed view of the streamwise development of the integral parameters, H, δ^* and θ is given in Figs. 8 and 9. After a steady rise in the boundary layer, the shape factor remains at a more or less constant value of about 3.2 in the wake up to $x = 85$ mm. The nearly constant value of H indicates a nearly constant centreline velocity in that region. For larger values of x the shape factor increases again. Clearly, for trailing-edge distances up to $x = 175$ mm, the present wake shows no tendency to attain a self-similar behaviour, which is characterized by a constant shape factor.

The momentum thickness increases towards the trailing edge due to the effects of the skin-friction and the adverse

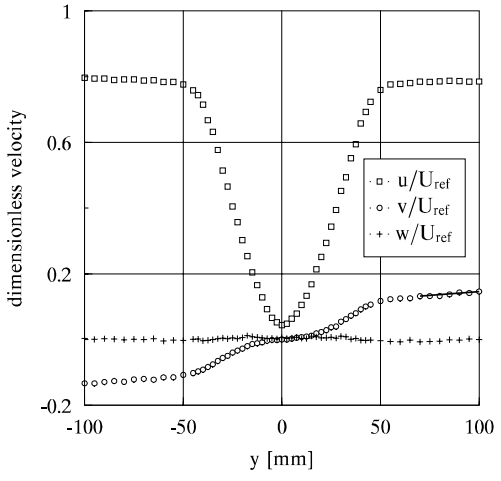

Fig. 6. Components of the mean velocity at $x = 53$ mm. The line drawn between $70 < y < 100$ is the $\bar{v}$ distribution that is computed from the static-pressure measurements and the continuity equation.

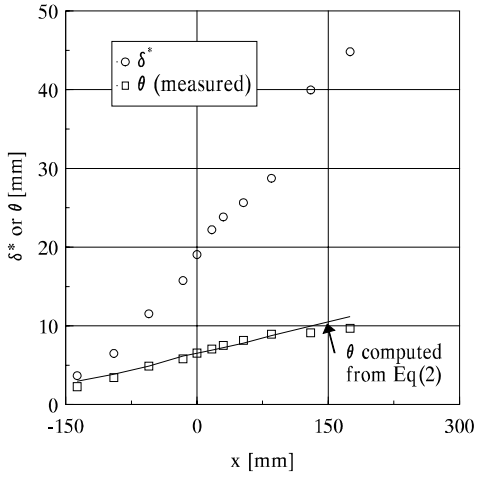

Fig. 8. Streamwise development of integral parameters δ^* and θ.

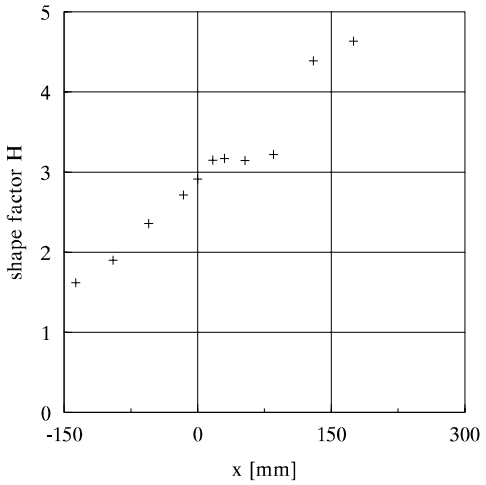

Fig. 9. Streamwise development of the shape factor $H \equiv (\delta^*/\theta)$.

pressure gradient. The latter alone causes the increase of the momentum thickness in the wake. The integral momentum equation was used to assess the self-consistency of the experimental data, despite the fact that the integral momentum equation is based on the "thin-shear-layer" approximation so that its accuracy is questionable in this particular flow. The integral momentum equation

$$\frac{\mathrm{d}\theta}{\mathrm{d}x} = -(2+H)\frac{\mathrm{d}U_\mathrm{e}}{\mathrm{d}x}\frac{\theta}{U_\mathrm{e}} + \frac{C_\mathrm{f}}{2} + \frac{1}{U_\mathrm{e}^2}\frac{\mathrm{d}}{\mathrm{d}x}\int_0^\infty (\overline{u'^2} - \overline{v'^2})\,\mathrm{d}y \tag{2}$$

was integrated with respect to x using the experimental values of the shape factor H, the static-pressure coefficient C_p and the skin-friction coefficient C_f. Details on the measurement of the skin friction will be discussed below. The constant of integration was chosen such that the inferred distribution of θ matched the measured distribution at the trailing edge $x = 0$. The results of this procedure are shown in Fig. 8 as a solid line. Two comments on the development of the momentum thickness are relevant. First, the inclusion of the last term on the right-hand side of Eq. (2), i.e. the term that incorporates the effect of the streamwise development of Reynolds stresses, is important in this wake. Without this term the computed values of θ would increase at a much slower rate than in the experiments. (The term accounts for approximately 30% of $\mathrm{d}\theta/\mathrm{d}x$ in the wake.) Secondly, the pressure-gradient term is much larger than the skin-friction term in the region of the flow that is covered by the experiments. As a result, the contribution of the skin friction to the growth rate of θ is very small, which is essentially different from the zero-pressure-gradient boundary layer.

3.2.2. Skin-friction data

The skin-friction coefficient C_f was determined by means of the Clauser-chart method. Fig. 10 portrays the Clauser charts for each boundary-layer station. It is well known that errors in the determination of the wall distance of the LDA measuring volume can have large effects on the outcome of the Clauser-chart method (see e.g. Absil and Passchier, 1994). In the present experiment the wall distance could be determined with an inaccuracy of ± 0.03 mm. The horizontal error bars in the Clauser chart for station $x = -137$ mm indicate that a ± 0.03 mm error will have a negligible effect on the outcome of the matching procedure. Also shown in the Clauser chart for $x = -137$ mm are the curves for $C_\mathrm{f} = 0.0026 \pm 0.0002$ to indicate the sensitivity of the matching procedure to variations in the selected value of C_f.

For $x = -137$ mm it is seen that Reichardt's formulation of the law of the wall (full line in Fig. 10)

$$u^+ = \frac{1}{\kappa}\ln(1+\kappa y^+) + \frac{C\kappa - \ln\kappa}{\kappa}\left(1 - \mathrm{e}^{\frac{-y^+}{11}} - \frac{y^+}{11}\mathrm{e}^{-0.33y^+}\right) \tag{3}$$

agrees well with the experimental data up to $y^+ \approx 50$. This range of y^+ values does not include the logarithmic region of Reichardt's mean-velocity distribution. The absence of any noticeable logarithmic behaviour of the measured mean-velocity profile is not surprising considering the relatively small value of R_θ. At $x = -137$ mm the value of R_θ is 1430. It is known from DNS studies, for example Spalart (1988), that the boundary layer on a flat plate in zero-pressure-gradient has only a small logarithmic region at this Reynolds number (roughly between $y^+ = 30$ and $y^+ = 150$). In addition to the effect of the low Reynolds number, there is the effect of the adverse pressure gradient. As can be seen from Fig. 10, the discrepancy between Reichardt's mean-velocity distribution and the experimental data increases when approaching the trailing edge. The discrepancy increases especially near the outer region, and it has a tendency to propagate into the inner region. For example, at $x = -95$ mm there is good overlap up to $y^+ = 30$, but at the trailing edge ($x = -0$ mm) it has become practically impossible to match Reichardt's velocity distribution to the experimental data. This underlines the basic weakness of the Clauser-chart method: the reliance on the validity of the law of the wall. It is unrealistic to expect that the mean-velocity distribution in a boundary layer that is in strong non-equilibrium can be described by a law of the wall. Consequently, the skin-friction coefficients that follow from the Clauser charts become increasingly unreliable when moving towards the trailing edge. Unfortunately, it was not possible to determine the friction velocity directly from the slope of the mean-velocity profiles at the wall, because the minimum wall distance for the boundary-layer traverses is approximately 0.3 mm, corresponding to $y^+ \approx 6$.

3.2.3. Centreline velocity

It is seen from Fig. 7 that, in addition to an increase of the width of the wake, the wake defect increases in the downstream direction. A detailed view of the mean velocity on the wake centreline, $\bar{u}_\mathrm{cl}$, is shown in Fig. 11. The graph shows that there is an initial increase of the centreline velocity in the region between the trailing edge (where

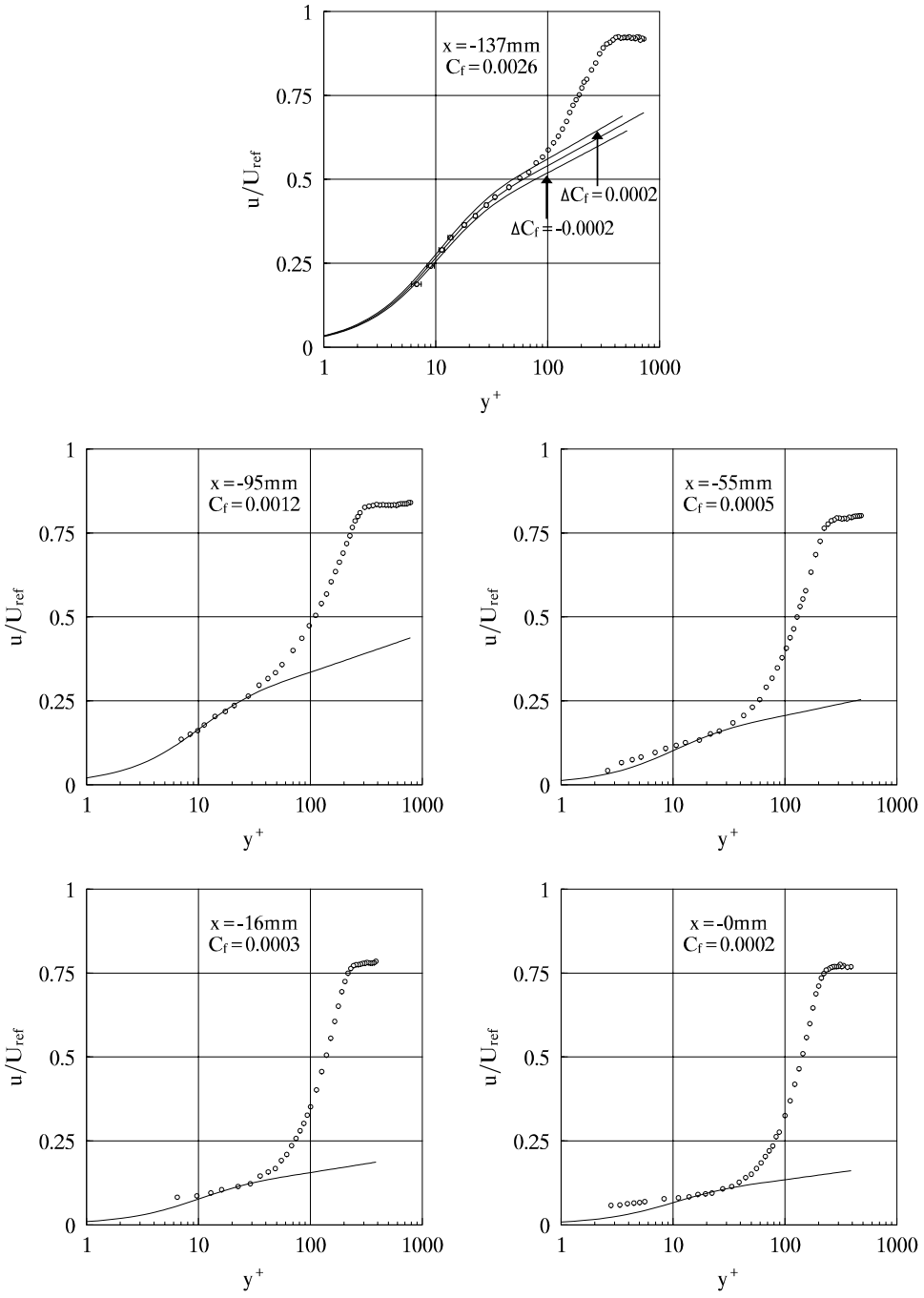

Fig. 10. Clauser charts for different boundary-layer stations.

$\bar{u}_{cl} = 0$) and the first measuring point at $x \approx 2$ mm. This is followed by a gradual decrease of the centreline velocity and a backflow region is formed downstream of $x \approx 80$ mm. The centreline velocity decreases to about $-0.15U_e$ at the measurement station farthest downstream. Because the pressure gradient relaxes beyond $x \approx 400$ mm, the mean velocity will increase further downstream. However, this region was not covered by the present experiment.

Also plotted in Fig. 11 are the results for the zero-pressure-gradient wake measured by Starke (2002), who used the same wake generator and experimental facility as in the present investigation. Starke's data clearly show a logarithmic behaviour of the centreline velocity for large trailing-edge distances, which is a characteristic of the constant-pressure wake of a flat plate (see e.g. Alber, 1980). A qualitative explanation for the large differences between the two wakes follows from the Reynolds-averaged momentum equation. For the x-direction this equation reads

$$\bar{u}\frac{\partial \overline{u}}{\partial x} + \bar{v}\frac{\partial \overline{u}}{\partial y} = -\frac{1}{\rho}\frac{\partial \overline{p}}{\partial x} - \frac{\partial \overline{u'^2}}{\partial x} - \frac{\partial \overline{u'v'}}{\partial y} + \nu\left(\frac{\partial^2 \overline{u}}{\partial x^2} + \frac{\partial^2 \overline{u}}{\partial y^2}\right). \quad (4)$$

Of course, $\overline{v} = 0$ along the centreline. Furthermore, the viscous terms can be neglected some distance from the trailing

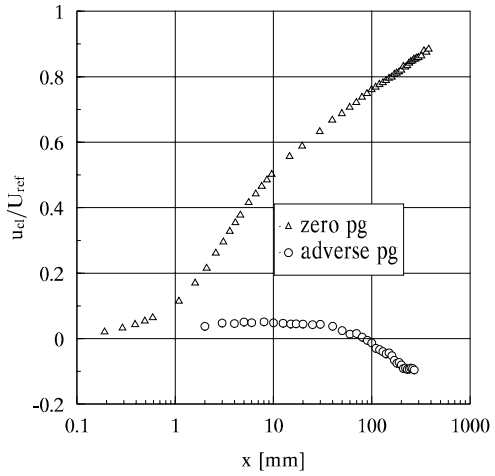

Fig. 11. Mean velocity on the centreline for two pressure gradients.

edge. In the zero-pressure-gradient wake the centreline velocity rapidly increases owing to the large gradient in Reynolds shear stress. The shear-stress gradient is smaller in the adverse pressure-gradient wake. In addition, the adverse pressure gradient stimulates the streamwise growth of the Reynolds normal stress. This opposes the tendency of the shear-stress gradient to accelerate the mean flow. In the present wake, the combined effects of the adverse pressure gradient and the two Reynolds-stress gradients have apparently resulted in a small increase of the maximum velocity defect instead of the rapid decrease that is found in case of a mild adverse or zero pressure gradient.

Interestingly, the mean-flow reversal begins some distance downstream of the trailing edge at $x \approx 80$ mm. This means that "free separation" takes place, since the recirculation zone is detached from the surface of the plate. Clearly, the mean-flow reversal occurs because the adverse pressure gradient increases the maximum velocity defect of the wake. The decrease of the centreline velocity is preceded by an initial increase directly downstream of the trailing edge. The explanation for this initial increase of the centreline velocity follows from Fig. 12, which shows the mean velocity in the boundary layer at the trailing edge ($x = -0$ mm). As mentioned before, this boundary layer is close to separation. The mean-velocity profile has a wake-like shape, except for a thin region directly above the wall. In this region, the mean velocity rapidly increases from zero at the wall to $0.07U_e$ at $n \approx 2$ mm. The relatively high turbulent viscosity in this region is responsible for the increase of the centreline velocity directly downstream of the trailing edge. Therefore, one may speculate that if the boundary layer were separated at the trailing edge, then there would not have been an initial rise of the centreline velocity. Consequently, a more conventional recirculation zone would have occurred with negative centreline velocities occurring immediately downstream of the trailing edge.

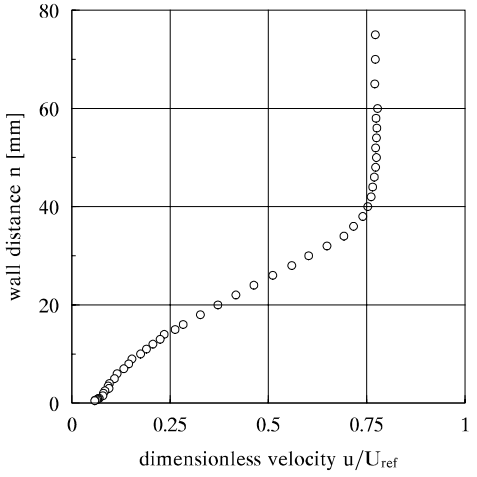

Fig. 12. Mean-velocity distribution at the trailing edge ($x = -0$ mm).

3.3. Turbulence quantities

3.3.1. Reynolds stresses

Recall that two coordinate systems are used in this investigation. In the boundary layer the s,n,z-coordinate system is used with axes parallel and normal to the plate surface. The wind-tunnel axes (x,y,z) are used as a coordinate system in the wake. The (kinematic) Reynolds shear stress, $-\overline{u'v'}$, is dependent on the orientation of the coordinate system, and as a consequence, there will be unrealistic variations in the shear-stress profiles at the trailing edge, where the coordinate system changes from wall orientation to tunnel-axis orientation. To avoid these problems, the Reynolds stresses were transformed into local streamline coordinates according to (see Cutler and Johnston, 1984)

$$\overline{u'v'_s} = \overline{u'v'}\cos(2\alpha) - \frac{1}{2}(\overline{u'^2} - \overline{v'^2})\sin(2\alpha), \tag{5}$$

where α is the angle between the mean-velocity vector and the x-axis given by $\alpha = \tan^{-1}(\overline{v}/\overline{u})$. Clearly, high growth rates of the shear-layer result in relatively high values of α. The development of $-\overline{u'v'_s}$ is shown in Fig. 13. For the most upstream station, there is little difference between

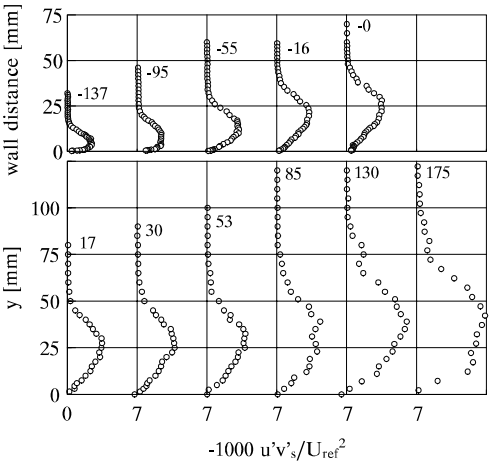

Fig. 13. Streamwise development of the Reynolds stress $-\overline{u'v'_s}$. Top: boundary layer, bottom: wake.

$\overline{u'v'_s}$ and $\overline{u'v'}$, because there the boundary layer thickens only slowly. However, near the trailing edge and in the wake the growth rate of the shear layer has increased dramatically, so that $\overline{u'v'_s}$ and $\overline{u'v'}$ are quite different.

The Reynolds normal stresses were summed as $(\overline{u'^2} + \overline{v'^2} + \overline{w'^2})/2$ to yield the kinetic energy of the velocity fluctuations, k. Of course, k is an invariant quantity so that a coordinate transformation similar to Eq. (5) is unnecessary. The streamwise development of k is shown in Fig. 14. At station $x = -137$ mm the distribution of k has its maximum value very close to the wall. This peak gradually moves away from the surface as the flow approaches the trailing edge, in agreement with other experiments in a turbulent boundary layer approaching separation (see e.g. Simpson et al., 1981). The locations of the peaks practically coincide with the inflexion point of the mean-velocity profiles. As the flow moves past the trailing edge, the kinetic energy continues to rise in the downstream direction. Such a substantial growth of the kinetic energy is not observed in the constant-pressure wake of a flat plate. Usually, there is a slight initial increase of k when moving downstream of the trailing edge, but the "overshoot" is generally small (Hayakawa and Iida, 1992). The explanation for the large increase of the kinetic energy in the present wake is discussed later when the balance of the kinetic energy is considered.

A comparison of the results in Figs. 13 and 14 suggests that there is a similarity between the growth of the shear-stress profiles and the kinetic-energy profiles. The degree of similarity can be expressed by a "structural parameter," defined as

$$a_{sp} = \frac{-\overline{u'v'_s}}{k} \tag{6}$$

Experiments in zero-pressure-gradient boundary layers (see e.g. Townsend, 1976) suggest that $a_{sp} = 0.3$. For the present experiment the maximum value of a_{sp} for various stations in the boundary layer and the wake is plotted in Fig. 15. The value of a_{sp} is less than 0.3 for the range of x values that is covered by the experiments. However, it is likely that a_{sp} asymptotes to 0.3 for $x \ll -137$ mm.

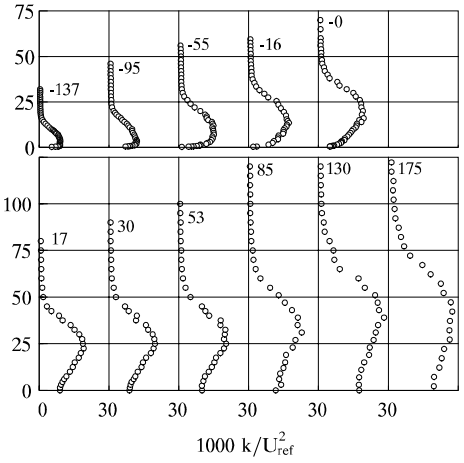

Fig. 14. Streamwise development of the kinetic energy k. Top: boundary layer, bottom: wake.

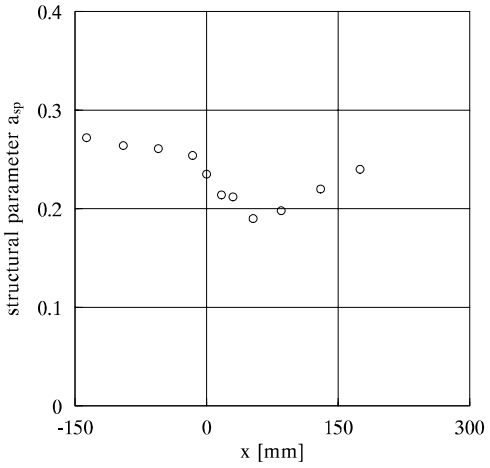

Fig. 15. The maximum value of the "structural parameter" for various stations in the boundary layer and the wake.

3.3.2. Reynolds-stress anisotropy

The contribution of the different Reynolds normal stresses to the kinetic energy can be defined as $\gamma_\alpha = \overline{u'^2_\alpha}/(2k)$. The quantity $2(\gamma_\alpha - 1/3)$ is a direct measure of the degree of anisotropy of the Reynolds stress $\overline{u'^2_\alpha}$. Fig. 16 gives the values of γ_α as determined from the centreline traverse. The full symbols followed from the lateral traverses at the intersection with the centreline, indicating the consistency of the data. Note that the tunnel-axis coordinates and the streamline coordinates coincide on the centreline of the wake, because of flow symmetry. As a result, there is no need for a transformation of the Reynolds stresses into local streamline coordinates.

It is seen in Fig. 16 that the contribution of the lateral fluctuations, $\overline{v'^2}$, to the kinetic energy is small close to the

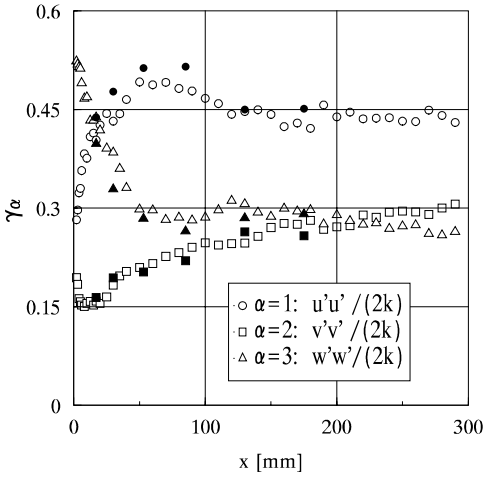

Fig. 16. The contribution of different Reynolds normal stresses to the kinetic energy along the centreline. The full symbols followed from the lateral traverses at the intersection with the centreline.

trailing edge, while the spanwise velocity fluctuations, $\overline{w'^2}$, are dominant in the same region. One of these observations can be explained as follows. Near the plate surface the lateral velocity fluctuations, $\overline{v'^2}$, are small compared to the streamwise fluctuations, $\overline{u'^2}$, and the spanwise fluctuations, $\overline{w'^2}$, owing to the wall blocking effect. Therefore, the contribution of $\overline{v'^2}$ to k at the trailing edge is small. However, this contribution is expected to increase in the wake once the wall constraint is removed at the trailing edge. Consistent with this reasoning, Fig. 16 indicates a small value of $\overline{v'^2}/(2k)$ near $x \approx 0$, with an increasing trend in the streamwise direction.

3.3.3. Triple-velocity correlations

The triple-velocity correlations were grouped as $\overline{u'q'} \equiv (\overline{u'^3} + \overline{u'v'^2} + \overline{u'w'^2})/2$ and $\overline{v'q'} \equiv (\overline{u'v'^2} + \overline{v'^3} + \overline{v'w'^2})/2$. As such, $\overline{u'q'}$ and $\overline{v'q'}$ are the x- and y-components of a vector which is related to the kinetic-energy transport. More precisely:

$$T_k = \frac{\partial(-\overline{u'q'})}{\partial x} + \frac{\partial(-\overline{v'q'})}{\partial y} \tag{7}$$

is the transport of turbulence kinetic energy by velocity fluctuations. In the present study all six triple-velocity correlations were measured, so that the components of the transport vector could be determined accurately.

The streamwise development of $-\overline{u'q'}$ and $-\overline{v'q'}$ is depicted in Fig. 17. The graph on the left-hand side shows that there is a strong growth of $-\overline{u'q'}$ in the streamwise direction. This indicates that the x-derivative of $-\overline{u'q'}$ in Eq. (7) may not everywhere be negligible compared to the y-derivative of $-\overline{v'q'}$, as is often assumed within the framework of the thin-shear-layer approximation. Another observation in Fig. 17 concerns the suitability of gradient-diffusion models for predicting the qualitative behaviour of the triple-velocity correlations in the present flow. For example, a standard k–ϵ model uses the following model for the triple-velocity correlations:

$$-\overline{u'q'} = \frac{\nu_t}{\sigma_k}\frac{\partial k}{\partial x} \tag{8}$$

for the x-direction and

$$-\overline{v'q'} = \frac{\nu_t}{\sigma_k}\frac{\partial k}{\partial y} \tag{9}$$

for the y-direction. In these expressions the effect of the pressure–velocity correlations on the transport of kinetic energy is neglected. Fig. 17 reveals slightly negative values of $-\overline{u'q'}$ near the wake centreline for $x > 130$ mm. This indicates counter-gradient transport, because the kinetic energy k continuously increases along the centreline. Apart from this small region near the centreline, the measured values of $-\overline{u'q'}$ are in qualitative agreement with Eq. (8). However, the situation is different for transport in the y-direction. In large parts of the wake and boundary layer the signs of the measured values of $-\overline{v'q'}$ are opposite to those predicted by the gradient-diffusion model (Eq. (9)). The only exceptions are the most upstream stations, where the boundary layer is still thin. There, the lateral transport of kinetic energy is described reasonably well by the gradient-diffusion model (qualitatively, at least) and the streamwise transport of kinetic energy is small compared to the lateral transport.

3.3.4. Balance of the momentum equation

Once the mean-velocity components and the Reynolds stresses are known from the experiment, one may attempt to evaluate the terms in the Reynolds-averaged momentum equation (Eq. (4)). To obtain the different lateral derivatives in momentum equation, polynomials were least-squares fitted to the measured profiles. Two successive y-traverses were used to determine the streamwise derivatives. The results of both wake halves were averaged to reduce the experimental scatter.

The individual terms in the momentum equation are shown in Fig. 18 for station $x = 30$ mm. The pressure-gradient term followed from the balance. Unfortunately,

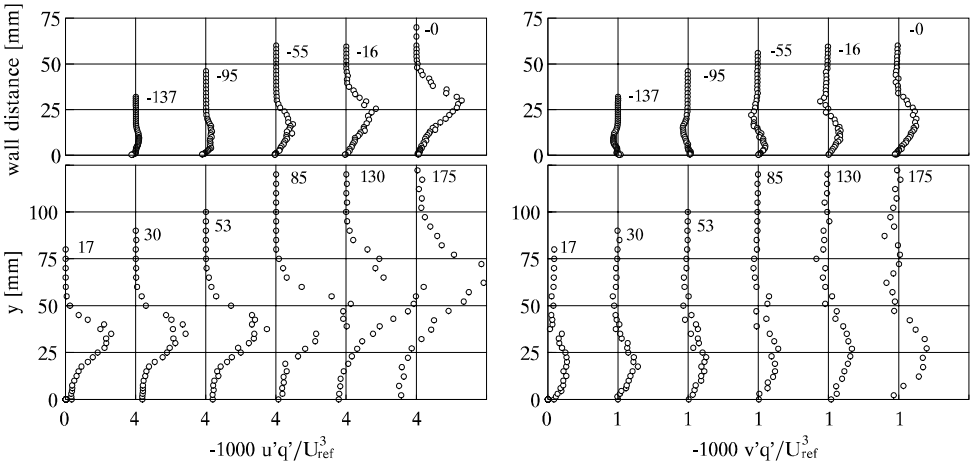

Fig. 17. Streamwise development of $-\overline{u'q'}$ (left) and $-\overline{v'q'}$ (right). Top: boundary layer, bottom: wake. The measured values of $-1000\overline{v'q'}$ at station $x = 17$ mm are shifted over 0.1.

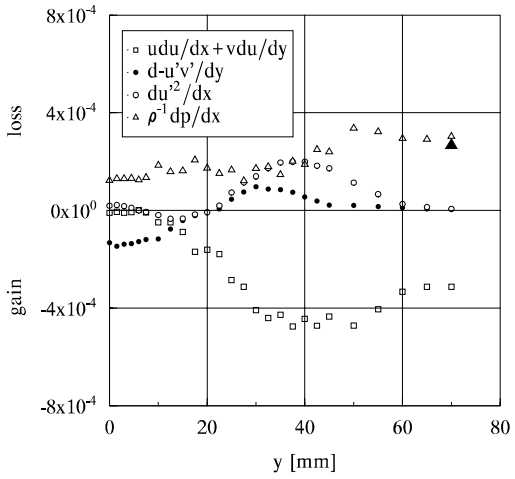

Fig. 18. Balance of the Reynolds-averaged momentum equation for the x-direction at station $x = 30$ mm. The full triangle represents the streamwise pressure gradient as determined from the static-pressure measurements outside the wake.

the variation in y-direction of this term could not be checked from independent measurements, because static pressures were not measured across the wake. The full triangle in Fig. 18 gives the streamwise pressure gradient as determined from the static-pressure measurements outside the wake.

The sum of the two Reynolds-stress gradients is locally larger than the pressure-gradient term. Therefore, the present wake is neither dominated by pressure forces nor is it dominated by turbulent stresses. The balance shows that both Reynolds-stress gradients are of equal importance. The effect of the Reynolds normal stress, $-\overline{u'^2}$, cannot be neglected compared to the effect of the Reynolds shear stress $-\overline{u'v'}$. Furthermore, it is seen that the streamwise growth of $\overline{u'^2}$ opposes the acceleration of the mean velocity near the centreline. There, all terms of the momentum equation have roughly the same magnitude and accurate modeling of all Reynolds stresses is required to predict the correct mean-flow behaviour.

3.3.5. Balance of the kinetic-energy equation

The experimental data were used to evaluate the terms in the kinetic-energy equation. The equation for the kinetic energy, k, is given by

$$\overline{u}_j \frac{\partial k}{\partial x_j} = -\overline{u'_i u'_j} \frac{\partial \overline{u}_i}{\partial x_j} - \epsilon + \frac{\partial}{\partial x_j}\left[-\frac{1}{2}\overline{u'_i u'_i u'_j} - \frac{1}{\rho}\overline{p' u'_j} + \nu \frac{\partial k}{\partial x_j}\right]. \tag{10}$$

Figs. 19 and 20 show the balances of the kinetic-energy equation at $x = 30$ mm and $x = 130$ mm, respectively. The effects of the molecular diffusion and the pressure diffusion on the transport of k are neglected. The viscous term is small in the wake so that its neglect has no serious consequences. As noted before, all six triple-velocity correlations were measured in the present study, so that the transport by the velocity fluctuations is described accurately. The dissipation ϵ was determined from the balance.

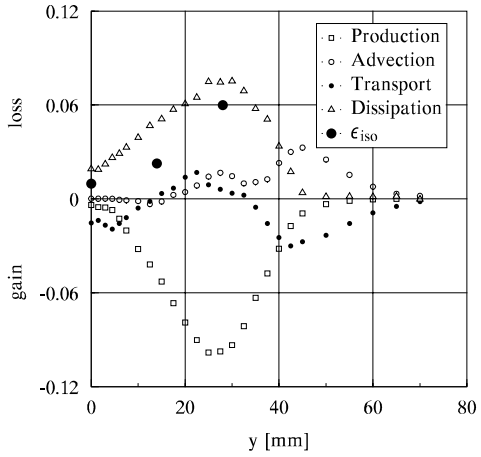

Fig. 19. Balance of the kinetic-energy equation at $x = 30$ mm. The large bullets are the isotropic values of the dissipation ϵ_{iso}.

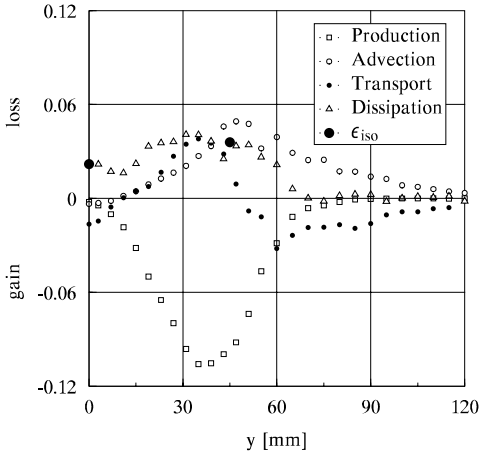

Fig. 20. Balance of the kinetic-energy equation at $x = 130$ mm. The large bullets are the isotropic values of the dissipation ϵ_{iso}.

At both stations the shear production is zero at the centreline due to flow symmetry, whereas the normal production is small due to the slowly varying mean velocity on the centreline. Integration of the transport profiles between $y = 0$ mm and the edge of the wake yields a non-zero value. This is the result of the streamwise derivatives of the triple-velocity correlations. Close to the centreline, the gain caused by the transport is balanced by the dissipation. The transport also causes the increase of the kinetic energy along streamlines near the edge of the wake.

It is seen from Figs. 19 and 20 that the approximate relation $\epsilon = P_k$ holds in the outer region of the wake. This relation underestimates the dissipation near the centreline and it overestimates the dissipation near the location of maximum production. The overestimation is especially large for the more downstream station. Both balances indicate that the wake is in strong non-equilibrium, because the production-to-dissipation ratios are significantly larger than one. Near the location of maximum production the ratios were determined as $P_k/\epsilon = 1.3$ for station

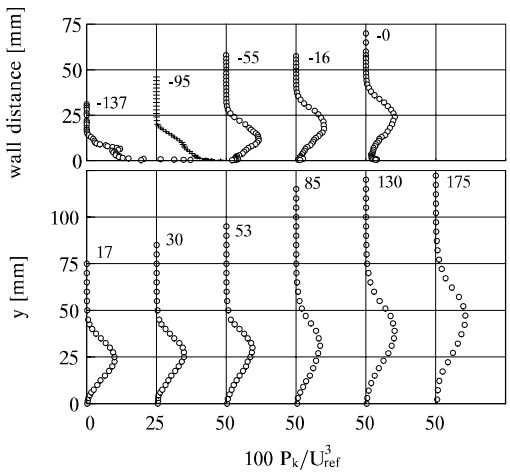

Fig. 21. Streamwise development of the production of turbulence kinetic energy, P_k.

$x = 30$ mm and $P_k/\epsilon = 2.6$ for station $x = 130$ mm. The development of the production of kinetic energy, as given in Fig. 21, goes some way in explaining the large increase of the production-to-dissipation ratio. (Note that a different symbol type is used in Fig. 21 for station $x = -95$ mm to avoid confusion with the neighbouring stations.) Fig. 21 shows that the peak values of P_k remain nearly constant in the wake. However, the total production of the kinetic energy, defined as the integral of P_k across the wake, continues to rise in the streamwise direction due to the widening of the P_k profiles. It appears that the increase of the production is not matched by a similar growth of the dissipation. Since the transport cannot cause an overall increase or decrease of the kinetic energy, it is inevitable that k steadily increases in the downstream direction.

A few comments on the accuracy of the kinetic energy balances should be made. First, the effect of the pressure–velocity correlation on the balance is neglected, because it cannot be measured. Secondly, the extraction of the transport term from the experimental data involves the differentiation of triple-velocity correlations. This is not an easy task considering the relatively high statistical scatter (±20%) in these correlations. However, at station $x = 30$ mm the inferred ϵ is positive everywhere and it has no unexpected indentations. At station $x = 130$ mm the ϵ distribution has unrealistic indentations at $y \approx 10$ mm and $y \approx 45$ mm. Also, ϵ becomes slightly negative near $y = 70$ mm. These errors are believed to be caused mainly by uncertainties in the transport term. However, the decrease of the dissipation level in the streamwise direction is confirmed by independent measurements of the dissipation. The dissipation values ϵ_{iso} in Figs. 19 and 20 were computed from

$$\epsilon_{iso} = 15\nu\overline{\left(\frac{\partial u'}{\partial x}\right)^2} = 30\nu\frac{\overline{u'^2}}{\lambda_x^2}, \tag{11}$$

where the Taylor length scale, λ_x, followed from two-point velocity correlation measurements (see Tummers, 1999 for details).

3.4. Anomaly of the spectral density functions in the wake

Spectral density functions (sdfs) of the velocity fluctuations in the x-direction were measured at various locations in the wake. The sdfs for four locations on the centreline between $x = 30$ mm and $x = 107$ mm are shown in Fig. 22. Four sdfs measured on a lateral traverse at $x = 130$ mm are given in Fig. 23.

The results in Fig. 22 indicate that there is little change in the high frequency part of the sdfs along the centreline of the wake. A striking feature of the sdfs is the presence of a "bump" for frequencies lower than approximately 25 rad/s. This low-frequency bump is relatively strong at $x = 30$ mm and gradually weakens farther downstream. The low-frequency bump is also visible in the sdfs measured on the lateral traverse at $x = 130$ mm (see Fig. 23). The strength of the bump appears to increase with increasing distance from the wake centreline.

It is interesting to explore the origin of the low-frequency content of the measured sdfs. If the largest turbulence structures of approximate size $\delta_{0.95}$ move past the measuring volume with velocity U_e, than this gives rise to a frequency of $\omega_1 = 2\pi U_e/\delta_{0.95} = 6.6 \times 10^2$ rad/s, when $U_e = 7.4$ m/s and $\delta_{0.95} = 70$ mm (these values pertain to station $x = 130$ mm). However, there are frequencies lower than ω_1 in a turbulent wake or boundary layer due to the presence of an interface that separates the turbulent air from the non-turbulent air. The location of the interface changes with time so that a (stationary) measuring volume is sometimes in the turbulent air and sometimes in the non-turbulent air. This intermittent behaviour of the flow results in frequencies as low as $\omega_2 = 0.1 \times \omega_1 = 6.6 \times 10^1$ rad/s (see e.g. Antonia et al., 1987). Clearly, even the lower frequency ω_2 is well outside the range of frequencies where the bump occurs: $\omega < 25$ rad/s. It can therefore be concluded that the intermittency of the flow cannot explain the observed low-frequency behaviour. For completeness, it is remarked here that the low-frequency bump in the sdfs is not an artifact of the experimental facility or the data-processing method. This follows from Fig. 24 which shows two sdfs measured in the near wake of the flat plate in zero pressure gradient using the same experimental facility and data-processing algorithm as in the present investigation.

In a further attempt to explain the low-frequency content of the spectral density functions it is useful to consider the effects of streamline curvature. Concave curvature can have large effects on a turbulent boundary layer (see e.g. Bradshaw, 1973). The degree of curvature is usually measured by the curvature parameter δ/r, where δ is the local thickness of the boundary layer and r is the local radius of curvature of the streamlines. According to Bradshaw (1973) concave curvature tends to destabilize the flow

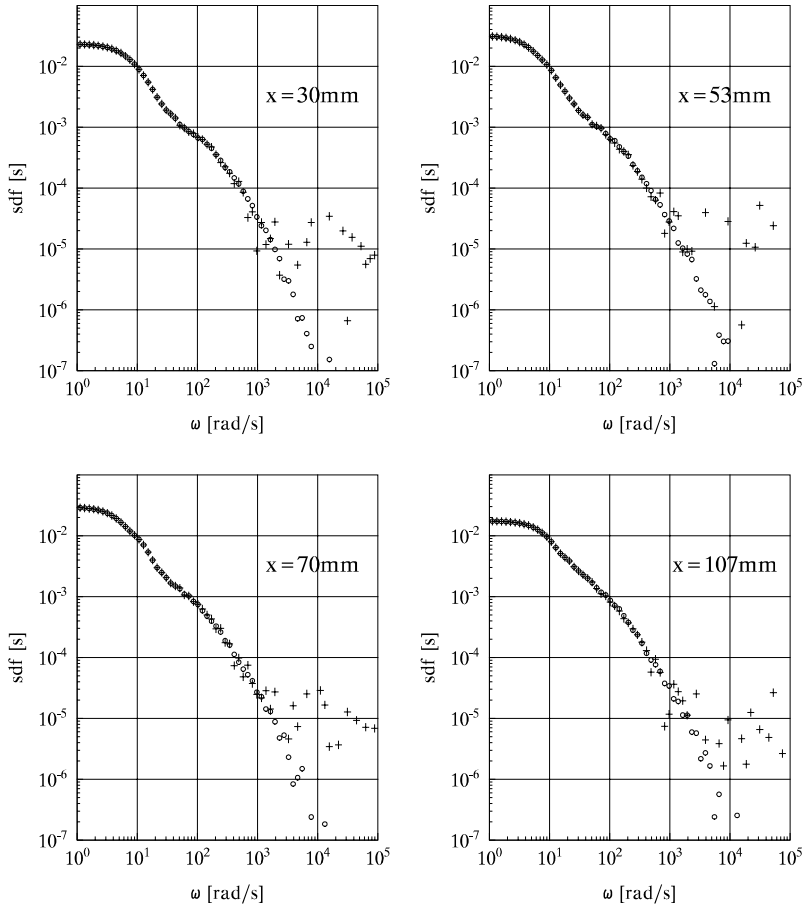

Fig. 22. Spectral density functions measured at various stations along the wake centreline.

and its effects are already noticeable for values of δ/r as small as 0.01.

The effects of concave curvature on the structure of a turbulent boundary layer were investigated by Jeans and Johnston (1982) and Barlow and Johnston (1988). In their experiments the curvature parameter δ/r varied between zero and 0.088. Flow visualisation with a laser light sheet and dye revealed that the concave curvature induced the formation of large-scale "roll cells" in the turbulent boundary layer with their axis in the mean-flow direction. These roll cells have their origin in the same centrifugal-instability mechanism that leads to the formation of Taylor–Görtler vortices in a concave laminar boundary layer. Clearly, if such roll cells have a stationary location in the turbulent boundary layer, they will give rise to a periodic variation in the spanwise direction of time-averaged quantities, i.e. a three-dimensional mean flow will occur. However, the experiments of Jeans and Johnston (1982) and Barlow and Johnston (1988) showed that the roll cells did not have a stationary behaviour. Instead, the roll cells grew, merged, disappeared and wandered in spanwise direction in a random manner so that long-term time averages were two-dimensional. However, the presence of the large-scale roll cells in the turbulent boundary layer introduced velocity fluctuations with very large time scales. More precisely, the spectral measurements of Barlow and Johnston (1988) showed that the differences between the flat and the curved boundary layer were confined to the very low-frequency range. The high-frequency content of the power spectra was hardly affected by the concave curvature.

In the present experiment in the adverse pressure-gradient wake, the surface of the wake generating plate is not curved except for a small region with convex curvature where the tapered trailing edge begins. However, the streamlines in the trailing-edge region are curved as a result of the rapid increase of the shear-layer thickness. The local radius of curvature of the streamlines r can be determined from the mean-velocity measurements using the following approximate expression (see Fig. 25):

$$r = \frac{\sqrt{(x_b - x_a)^2 + (y_b - y_a)^2}}{\tan(\gamma_b - \gamma_a)}. \tag{12}$$

Here, γ_a (γ_b) is the angle between the mean-velocity vector at location A (B) and the x-axis. The numerator in Eq. (12) is the distance between A and B.

For example, with A located on the boundary layer traverse at $x = -95$ mm and B located at $x = -55$ mm, a typical value of the radius of curvature was determined as $r \approx 1.1$ m. This yields a curvature parameter $\delta/r \approx 0.025$ when δ is evaluated as the average value of $\delta_{0.95}$ at stations $x = -95$ mm and $x = -55$ mm. Fig. 26 shows the

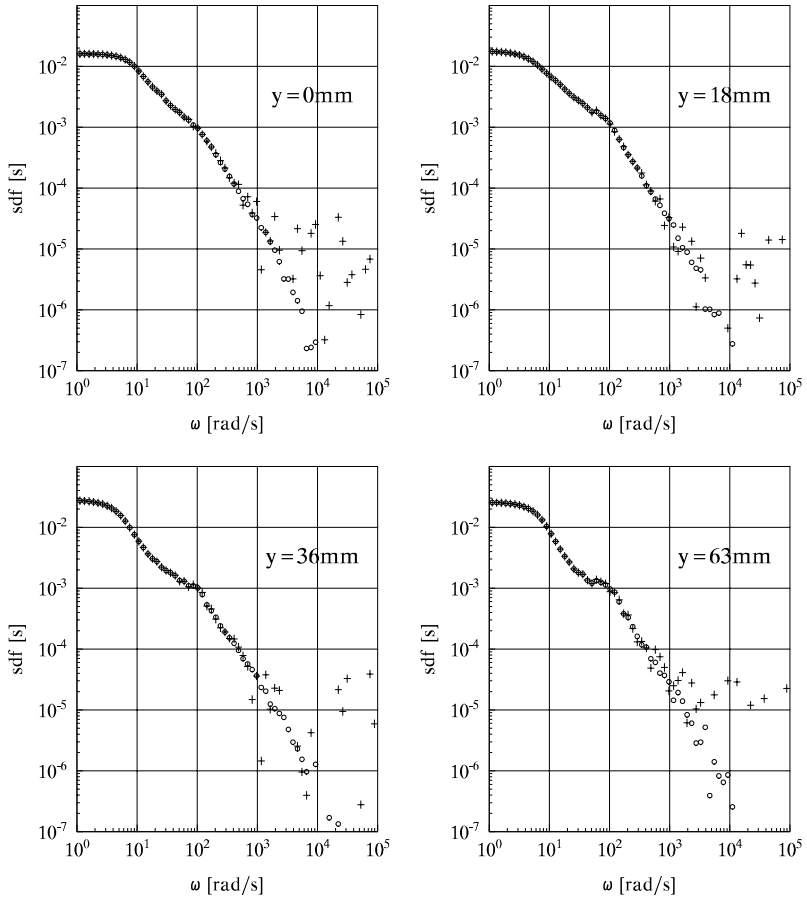

Fig. 23. Spectral density functions measured at station $x = 130$ mm. The local shear-layer thickness $\delta_{0.95}$ is approximately 70 mm.

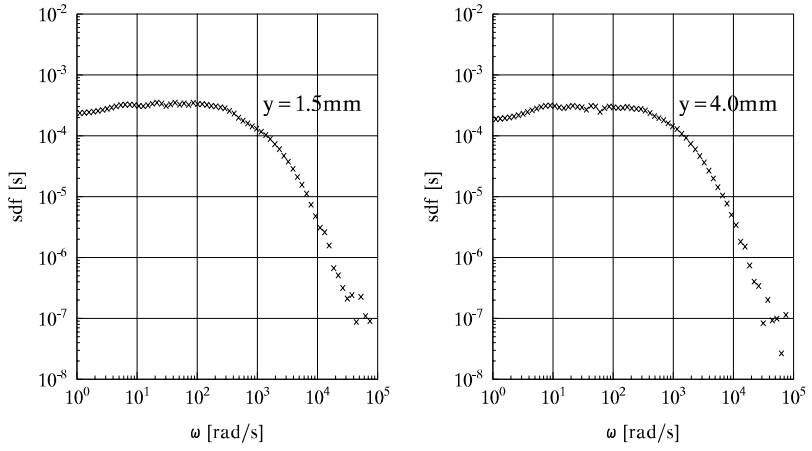

Fig. 24. Spectral density functions measured in the *zero-pressure-gradient* wake at a station 10.01 mm downstream of the trailing edge. The shear-layer thickness $\delta_{0.95}$ at this particular station is approximately 14 mm.

(dimensionless) angular momentum $r(\overline{u}^2 + \overline{v}^2)^{1/2}/(cU_{\mathrm{ref}})$ in the boundary layer at station $x = -95$ mm. It is seen that the angular momentum decreases towards the wall, i.e. the angular momentum decreases in the direction away from the centre of curvature as is the case in concave curvature. This concave curvature tends to destabilize the flow. Furthermore, a curvature parameter with a value of 0.025 can be interpreted as a moderate degree of curvature (Bradshaw, 1973).

An analysis of the mean-velocity data indicated that the streamlines were concavely curved at the other boundary-layer stations as well. Interestingly, the radius of curvature changes sign downstream of the trailing edge of the plate. For example, in between the wake stations $x = 30$ mm and $x = 53$ mm the curvature parameter is $\delta/r \approx -0.019$. There, the curvature of the streamlines is convex and tends to stabilize the flow. The effects of convex curvature on the flow are much smaller than that of concave curvature

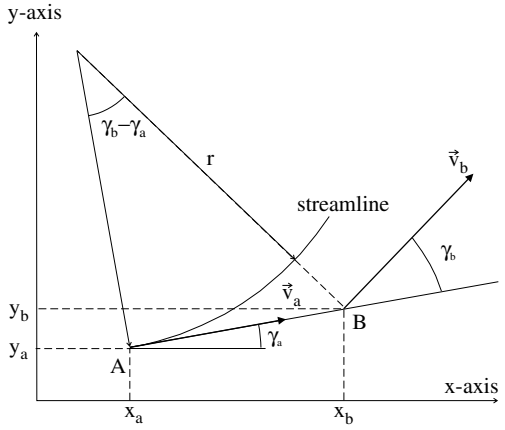

Fig. 25. Determination of local radius of curvature from mean-velocity measurements.

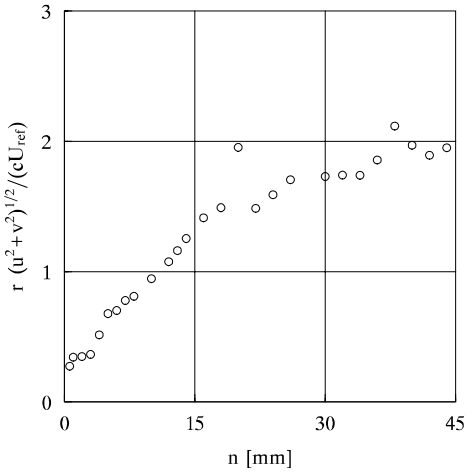

Fig. 26. The dimensionless angular momentum $r(\overline{u}^2+\overline{v}^2)^{1/2}/(cU_{\mathrm{ref}})$ as a function of the wall distance at boundary-layer station $x=-95$ mm.

(Bradshaw, 1973). Farther downstream the radius of curvature changes sign again; the value of δ/r in between stations $x=85$ mm and $x=130$ mm was determined as approximately 0.011.

It is now reasonable to speculate as follows. The rapid increase of the thickness of the boundary layer towards the trailing edge of the plate has resulted in streamlines with concave curvature. The concave curvature (with $\delta/r\approx 0.025$ in between station $x=-95$ mm and $x=-55$ mm) may have affected the structure of the boundary layer in the trailing-edge region through the formation of roll cells. The roll cells contain a significant amount of low-frequency energy, which appears in the measured spectral density functions as a bump in the low-frequency range (see Figs. 22 and 23).

Just downstream of the trailing edge the streamline curvature is convex so that there is no drive for the formation of roll cells. Also, the streamline curvature on the wake centreline is zero because of flow symmetry. This may explain the change in shape of the sdfs that were measured on the centreline (shown in Fig. 22). The bump in the low-frequency range gradually decreases with increasing distance from the trailing edge, indicating the gradual fading of the roll cells along the centreline. The sdfs that were measured on the lateral traverse at $x=130$ mm (shown in Fig. 23) indicate that the relatively small bump in the low-frequency range at $y=0$ mm increases with increasing y. This suggests that the remnants of the roll cells that were formed in the boundary layer are convected downstream by the mean flow. As a result, the roll cells also appear in the near wake especially in the outer regions, and, for sufficiently small trailing-edge distances, the effect of the rolls cells is also felt at the wake centreline.

Although the presence of the roll cells is speculative, the accumulation of a significant amount of kinetic energy in the low-frequency range is not. This spectral anomaly will have important consequences for the ability of RANS methods to predict the "free separation" in the present adverse pressure-gradient wake. This is the topic of an accompanying paper (Tummers et al., submitted for publication).

4. Conclusion

The experiments in the turbulent trailing-edge flow of a "thick" flat plate in an adverse pressure gradient indicate a rapid growth of the shear-layer thickness in the streamwise direction. The boundary layer on the plate remained attached, although it is close to separation at the trailing edge. After a slight initial increase, the mean velocity on the centreline decreases so that a region with mean-flow reversal is formed some distance downstream of the trailing edge, simulating the "free separation" phenomenon. The turbulence kinetic energy steadily rises in the downstream direction along the centreline. The measured balances of the kinetic-energy equation show the importance of transport by turbulent velocity fluctuations in the present wake, especially near the edges. The balances also indicated a significant decrease of the dissipation in the streamwise direction while the production of turbulence kinetic energy remains nearly constant. Power spectra measured in the wake revealed the presence of a significant amount of turbulence kinetic energy in the very-low-frequency range; a phenomenon not seen in the zero-pressure-gradient wake of the same flat plate. It is speculated that this is caused by the formation of "roll cells" in the turbulent shear layer as a result of concave streamline curvature.

References

Absil, L.H.J., 1995. Analysis of the laser doppler measurement technique for application in turbulent flows. Ph.D. Thesis, Delft University of Technology.

Absil, L.H.J., Passchier, D.M., 1994. An experimental study of the trailing edge flow of an nlr 7702 airfoil, using laser-doppler anemometry. Exp. Therm. Fluid Sci. 9 (2), 174–185.

Adair, D., Horne, W.C., 1989. Turbulent separated flow over and downstream of a two-element airfoil. Exp. Fluids 7 (8), 531–541.

Alber, I.E., 1980. Turbulent wake of a thin, flat plate. AIAA J. 18 (9), 1044–1051.

Antonia, R.A., Browne, L.W.B., Fulachier, L., 1987. Average wavelength of organised structures in the turbulent far wake of a cylinder. Exp. Fluids 5, 298–304.

Barlow, R.S., Johnston, J.P., 1988. Structure of a turbulent boundary layer on a concave surface. J. Fluid Mech. 191, 137–176.

Bradshaw, P., 1973. Effects of streamline curvature on turbulent flow. In: AGARD AG-169.

Cutler, A.D., Johnston, J.P., 1984. An experimental investigation of the effect of initial shear stress distribution on a separating turbulent boundary layer. In: AIAA Paper 1583, 17th Fluid Dynamics, Plasma Dynamics, and Lasers Conference.

Driver, D.M., Mateer, G.G., 2002. Wake flow in adverse pressure gradient. Int. J. Heat Fluid Flow 23, 564–571.

Hayakawa, M., Iida, S., 1992. Behaviour of turbulence in the near wake of a thin flat plate at low Reynolds numbers. Phys. Fluids A 4 (10), 2282–2291.

Hill, P.G., Schaub, U.W., Senoo, Y., 1963. Turbulent wakes in pressure gradients. J. Appl. Mech. 30 (12), 518–524.

Hoffenberg, R., Sullivan, J.P., 1998. Measurement and simulation of a decelerated wake. In: AIAA-98 Paper 0522.

Jeans, A.H., Johnston, J.P., 1982. The effects of streamwise concave curvature on turbulent boundary layer structure. Report md-40, Thermosciences Division—Department of Mechanical Engineering, Stanford University, USA.

Johnston, L.J., Horton, H.P., 1986. An experimental study of turbulent wake/boundary layer mixing flows. In: Proceedings of the International Congress of Aeronautical Sciences (ICAS), pp. 360–369.

Liu, X., Thomas, F.O., Nelson, R.C., 2002. An experimental investigation of the planar turbulent wake in constant pressure gradient. Phys. Fluids 14 (8), 2817–2838.

Nakayama, A., Kreplin, H.P., Morgan, H.L., 1990. Experimental investigation of flow field about a multielement airfoil. AIAA J. 28 (January), 14–21.

Petrov, A.V., 1980. Some features of flow past slotted wings. Library translation 2050, Royal Aircraft Establishment (also Uchenye Zapiski, TsAGI, 8,6, 1977, pp. 119–124).

Plomp, A., 1986. Characteristics of four aerosol generators for velocity measurements in a wind tunnel. Contract report 86/11, ECN, The Netherlands.

Simpson, R.L., Chew, Y.T., Shivaprasad, B.G., 1981. The structure of a separating turbulent boundary layer. Part 1: mean flow and Reynolds stresses. J. Fluid Mech. 113 (part 1), 23–51.

Spalart, P.R., 1988. Direct simulation of a turbulent boundary layer up to $r_\theta = 1410$. J. Fluid Mech. 187, 61–98.

Starke, A.R., 2002. A combined experimental and numerical study of the turbulent wake. Ph.D. Thesis, Delft University of Technology.

Townsend, A.A., 1976. The Structure of Turbulent Shear Flow, second ed. Cambridge University Press.

Tummers, M.J., 1999. Investigation of a turbulent wake in an adverse pressure gradient using laser doppler anemometry. Ph.D. Thesis, Delft University of Technology.

Tummers, M.J., Passchier, D.M., Henkes, R.A.W.M., 1997. Experimental investigation of an adverse pressure gradient wake and comparison with calculations. Exp. Thermal Fluid Sci. 14, 17–24.

Tummers, M.J., Hanjalić, K., Passchier, D.M., Henkes, R.A.W.M., submitted for publication. Computations of a turbulent wake in a strong adverse pressure gradient. IJHFF, submitted for publication.